The structure-activity interactions of Cu/Zn, In/Pd and Fe/K catalysts supported on mesoporous SBA-15; CO$_2$ Hydrogenation at Low Pressure

Zane Abelniece (✉ zaneabelniece@gmail.com)

Riga Technical University

Maria Giorgia Cutrufello

University of Cagliari

Elisabetta Rombi

University of Cagliari

Agija Stanke

Riga Technical University

Helle-Mai Piirsoo

University of Tartu

Hugo Mändar

University of Tartu

Aile Tamm

University of Tartu

Research Article

Abstract

To minimize greenhouse gas emissions, efficient carbon dioxide capture and utilization need to be addressed. In this study, to determine the structure-activity interplay, three different promising catalytic systems for the CO_2 hydrogenation process were synthesized using mesoporous silica SBA-15 as a support material: copper-based catalyst with zinc, indium-based catalyst with palladium and iron-based catalyst with potassium. The role of metal–metal oxide interaction has been showed. The use of Cu/Zn catalytic system and SBA-15 allowed to obtain very small crystallite size of tenorite and zinc oxide, good dispersion of active phases with strong basic sites. In order to find the most effective catalyst providing the maximal methanol yield and selectivity, these catalytic systems were compared under the same reaction conditions (250°C, 20 bar, H_2 to CO_2 molar ratio 4 to 1) using fixed-bed tubular micro-activity reactor. Results showed that the highest methanol yield can be obtained with Cu/Zn/SBA-15 catalyst as might be expected according to obtained characterization.

1. Introduction

The amount of greenhouse gases in the atmosphere increases leading to adverse effects on environment and climate. Currently, the amount of carbon dioxide (CO_2) emission exceeds the levels adopted in the Paris Agreement. To reduce the negative effects of greenhouse gases on the environment, more efficient utilization of fossil fuels as well as CO_2 capture and utilization need to be addressed. Carbon capture, utilization, and storage is an emissions reduction technology that has attracted a great attention in recent years due to its high efficiency [1]. One of the carbon utilization methods is the catalytic hydrogenation of CO_2 which converts CO_2 into energy products, such as methanol. Methanol has a wide range of applications: it can be used to produce a variety of chemicals and it is also an alternative fuel. Today, methanol is mainly synthesized in an industrial process from fossil sources using $Cu/ZnO/Al_2O_3$ catalysts, that converts synthesis gas ($H_2/CO/CO_2$) into methanol under rather harsh conditions (at a pressure of 50–100 bar and a temperature of 200–300°C). In recent years the interest of direct hydrogenation to methanol has increased significantly. The catalytic hydrogenation of CO_2 is green and environmentally-friendly method, especially if the cost-effective and safe conditions are applied [2].

Effective catalyst is a key parameter to CO_2 hydrogenation performance. The most efficient catalysts for CO_2 hydrogenation to methanol are multi-component catalytic systems consisting of intermixed metal and metal oxides nanoparticles.

The most effective/promising catalytic systems for CO_2 hydrogenation to methanol reported in the literature are copper-zinc oxide based catalysts, indium oxide-palladium based catalysts [2] and iron-potassium based catalysts [3]. The complexity of the multi-component catalytic systems and challenges in elucidating the active sites are the main stumbling blocks in developing rational catalyst design strategies [2].

The main role of ZnO in Cu/Zn catalyst has been proposed to increase Cu dispersion, the exposure of more active Cu sites. ZnO prevents the agglomeration of Cu particles, thus leading to the large Cu surface area needed for methanol synthesis[4]. A large Cu surface area is important to obtain high activity, but there are differences in intrinsic activity between Cu/ZnO-based catalysts with different preparation history. Additionally, the fact that the migration of Zn species to Cu surface generates active sites, oxygen vacancies or Cu-Zn surface alloy may facilitate CO_2 hydrogenation to methanol [5].

Recently, In_2O_3-based catalysts with oxygen vacancies have been reported to possess higher methanol selectivity than Cu/Zn based catalysts [6,7,8]. Over the last decade, indium-based catalysts have gained significant interest for CO_2 hydrogenation to methanol, based on low activity for the reverse water–gas shift reaction, which results in high methanol selectivity over a wide temperature range. Ye et al. predicted that methanol formation is favorable on the defective $In_2O_3(110)$ surface containing oxygen vacancies [9]. In Jiang et al. work it was shown that the addition of Pd enhanced the number of oxygen vacancies on the surface of In_2O_3 and facilitated the CO_2 activation through interaction with In_2O_3 [6].

The synergistic effects of K (and Na) in the iron catalyst are responsible for the excellent higher alcohol synthesis [10,11]. As limited progress has been made in the hydrogenation of CO_2 to alcohols with iron catalysts, in this study Fe/K on SBA-15 was used to determine the activity in reactions. Xi et al. reported that well-dispersed Fe_2O_3 and In_2O_3 phases with oxygen vacancies can be observed on Ce-ZrO_2 support [3]. Potassium can greatly affect CO_2 and H_2 activation, thus regulating CO_2 conversion and product selectivity [11].

The thermodynamics of CO_2 conversion also limits methanol synthesis due to the competing reverse water-gas shift reaction. Furthermore the by-product water can have negative effects on the activity and stability of the catalyst during CO_2 hydrogenation to methanol [2]. The effective solution for the stabilization of the active phase/nanoparticles and improvement of catalytic and mechanical properties is the dispersion of the active phase onto a suitable, high-surface area support, such as SBA-15 (Santa Barbara Amorphous mesoporous silica). It is well-known that supports can increase active metal surface area and stabilize the particles from sintering thus improving the catalytic and mechanical properties [5]. SBA-15 ordered mesoporous structure allows the formation of active nanophases with narrow particle size distribution, the wall thickness ensures the thermal stability of the support, and the size of pores allows the easy diffusion of the gaseous molecules [4].

It was found in recent years that metal-support interaction and creation of interfacial sites promotes metal dispersion, and changes concentration of acid sites, basic sites, and oxygen vacancies on the catalyst surface [5]. Mureddu et al. studied CO_2 hydrogenation to methanol using Cu/Zn/Zr/SBA-15 catalyst and showed that strong metal–support interaction could prevent the restructuring effects of copper particles like particle agglomeration during the reaction [4]. The study revealed that better results can be achieved when a thin amorphous homogeneous layer of the active phase is formed, rather than

larger particles located at the external surface, leading to improved activity and selectivity of the catalyst [4].

In this study SBA-15 was applied as carrier material providing large surface to disperse the active components and to ensure the thermal stability during the reaction. SBA-15 has abundant mesopores beneficial to mass transferwhich makes it a promising catalyst support for industrial applications [12]. Besides, our previous study reveals that methanol yield obtained using Cu/ZnO/SBA-15 catalyst is comparable to the yield obtained with the commercial catalyst [13]. Three different promising catalytic systems for the CO_2 hydrogenation process were studied and the influence of metal – support interaction on the structure of catalysts and the activity of CO_2 hydrogenation reaction was investigated using mesoporous SBA-15 as a support material. These catalytic systems are: copper-based catalyst (with Zn), indium-based catalyst (with Pd) and iron-based catalyst (with K). These catalytic systems were compared at the same reaction conditions to find the most effective one providing the maximal methanol yield and selectivity.

Direct comparison of these catalysts with identical metal content under identical reaction conditions (fixed-bed tubular micro-activity reactor, 20 bar and the temperature 250°C) is performed for the first time for the development of more effective catalysts, which can promote commercialization of the CO_2 hydrogenation process.

2. Materials And Methods

2.1. Preparation of Catalysts

SBA-15 (S) was purchased from ACS Material LLC and used as a carrier material for all three catalysts. Catalysts were prepared by co-impregnation method.

Cu/Zn/S: an aqueous solution (20 ml) with appropriate amount of $Cu(NO_3)_2 \cdot 2.5H_2O$ and $Zn(NO_3)_2 \cdot 6H_2O$ was made to obtain metal loadings: Cu 20% and Zn 7%. The solution was added dropwise to 1.05 g of S, then mixed and heated for 2 h, and finally treated in ultrasound bath for 2 h. Afterwards the solid obtained was dried overnight at 90°C and then calcined in a muffle furnace at 400°C for 4 h. Cu/Zn molar ratio is 3.2.

In/Pd/S: 10 mL of aqueous solution of $In(NO_3)_3 \cdot 3H_2O$ was mixed with 10 mL of aqueous solution of $Pd(NO_3) \cdot 2H_2O$ (metal loadings: In 20% and Pd 6%). This solution was added dropwise to 1.05 g of S, then mixed and heated for 2 h, and finally treated in ultrasound bath for 2 h. Afterwards solid obtained was dried overnight at 90°C and then calcined at 400°C for 4 h. In/Pd molar ratio is 3.2.

Fe/K/S: 10 mL of aqueous solution of $Fe(NO_3)_3 \cdot 9H_2O$ was mixed with 10 mL of aqueous solution of KNO_3 (metal loadings: Fe 20% and K 1%). This solution was added dropwise to 1.05 g of S, then mixed

and heated for 2 h, and finally treated in ultrasound bath for 2 h. Afterwards solid obtained was dried overnight at 90°C and then calcined at 400°C for 4 h. Fe/K molar ratio is 13.

2.2. Characterization of Catalysts

X-ray diffraction analysis (XRD) of samples in both small angle scattering (SAXS) and wide angle scattering (WAXS) modes was performed on diffractometer SmartLab™ (Rigaku, Japan) using Cu rotating anode operated at 45 kV and 180 mA, and a coordinate sensitive 1D detector D/teX Ultra (WAXS range in reflection Bragg-Brentano optical scheme) or a scintillation detector (SAXS range implementing transmission SAXS optics). Diffraction patterns were measured between angles of 8 and 80° with step size of 0.02° (2θ) and scan speed of 5 deg min^{-1} (WAXS), or from 0.1 to 2.5° with step size of 0.01° (2θ) and scan speed of 0.26 deg min^{-1} (SAXS). Program *PDXL* (Rigaku) and ICDD database PDF-2 (2020) were used for identification of phases. X-ray apparent crystallite size was calculated from Scherrer equation. Instrumental broadening of reflections was determined on standard reference material SRM-660 (LaB_6).

The surface area and the pore size were determined by N_2 adsorption-desorption isotherms obtained using a Quantachrome Instruments Nova 1200 E-Series surface and porosity analyzer at $-196°C$. The samples were out-gassed at 150°C for 24 h before measurement. Total surface area was estimated by using the Brunauer-Emmett-Teller (BET) method. Pore diameters were derived from desorption isotherms using the Barrett-Joyner-Halenda (BJH) method.

Morphology and composition were studied using scanning electron microscope (SEM) (Helios Nanolab 600 by FEI) equipped with energy dispersive X-ray (EDX) analysis detector (INCA Energy 350 by Oxford Instruments). The structure of the catalysts was investigated with transmission electron microscope Titan Themis 200 (FEI) operating at 200 kV in scanning mode (STEM). The powdered sample was mixed with ethanol to make a suspension. Energy dispersive X-ray (EDX) spectroscopy was done with SuperX (Bruker) system in the same microscope.

Inductively coupled plasma atomic emission spectroscopy (ICP-AES) analyses were performed with a 5110 ICP-OES spectrometer (Agilent Technologies) to determine the chemical composition. To determine K, Fe, In, and Si contents, the samples were prepared as follows: after calcination at 300°C for 12 h, ca. 0.04 g of sample were mixed with lithium tetraborate (1:15 w/w), placed in a platinum crucible, and then fused at 1000°C in a furnace for 30 min. After cooling of the melt, the resultant fusion bead was dissolved at 80°C for about 30 min with 100 mL of a HNO_3 solution (0.80 M) and finally diluted to the desired volume with Milli-Q water. Pd amount was determined by treating ca. 0.05 g of sample with a mixture of HCl (37%) and HNO_3 (70%) (3:1 by volume) at 80°C for 3 h; after filtration, the solution was diluted to the desired volume with MilliQ water.

Temperature programmed reduction (TPR) was performed on a TPD/R/O 1100 apparatus (Thermoquest) equipped with a TCD detector, using ca. 0.05 g of sample. TPR runs were carried out with a H_2/Ar mixture (5 vol% of H_2, 30 mL/min) from 40 to 950°C (hold 30 min), with a heating rate of 10°C/min. Prior to

analysis, the samples were pretreated under flowing Ar (20 mL/min) at 300°C for 1 h. The amount of H_2 consumed was calculated after calibration of the TCD response using CuO as the standard.

Temperature programmed desorption of CO_2 (CO_2-TPD) was performed from 40 to 500°C (heating rate 10°C/min, hold 45 min) using He (20 mL/min) as the gas carrier. Prior to analysis, the samples (ca. 0.15 g) were saturated with pulses of pure CO_2 (pulse volume 0.347 mL) at 40°C under flowing He (50 mL/min). Prior to analysis, the samples were pretreated under flowing Ar (20 mL/min) at 300°C for 1 h. The TCD response was calibrated by performing a pulse calibration run (at 40°C, CO_2 pulse volume 0.347 mL, He flow rate = 20 mL/min) in an empty reactor.

2.3. Catalyst Testing

The CO_2 hydrogenation was performed in a fixed-bed stainless steel tubular micro-activity reactor (Microactivity-Effi, PID Eng&Tech S.L.). For each experiment, 0.2 g of catalyst mixed with sand to 3 mL volume was loaded in a catalyst bed above the quartz wool. The catalysts were reduced at atmospheric pressure under a flow of H_2 at flow rate of 50 mL min^{-1} at 350°C for Cu/Zn/S and Fe/K/S catalysts and at 200°C for In/Pd/S catalyst for 4 h. The temperature was lowered to 160°C; subsequently a flow of H_2 (99.995% purity), CO_2 (99.995%) and N_2 (99.9%) mixture (4:1:1) was fed through the reactor at a flow rate of 60 mL min^{-1}, similar like in our previous study [13]. The pressure was increased from atmospheric to 20 bar and the temperature from 160°C to 250°C. The time on stream after achieving the reaction temperature was 50 h. After leaving the reactor, the exit gas passed through cold trap ($T = 5°C$) to condense products. The reactor outlet gas composition was analysed on-line by a gas chromatograph (Shimadzu Nexis GC-2030) and the condensed products with infra-red spectrometer, the same as in [13].

The CO_2 conversion (X) and product distribution (D_{prod}) were calculated as follows:

$$X_{CO_2} = \left(\frac{nCO_{2in} - nCO_{2out}}{nCO_{2in}} \right) \times 100 \tag{1}$$

$$D_{prod} = \left(\frac{A_i}{\sum A_i} \right) \times 100 \tag{2}$$

where nCO_{2in} and nCO_{2out} is the number of moles of CO_2 at the inlet and outlet, respectively. A_i and ΣA_i represent the moles of selected product 'i' and total moles of all products, respectively.

The space time yield of methanol (STY) was calculated as follows:

$$STY_{CH_3OH} = m_{CH_3OH} / (m_{cat} \bullet t) \tag{3}$$

where m_{CH3OH} represents the total mass of methanol formed (g), t indicates the time of reaction (h), m is the mass of the catalyst (g).

Each experiment was carried out twice and the average value was calculated.

3. Results And Discussion

3.1. Elemental composition of catalysts

The elemental composition of the catalysts, determined by ICP-AES analysis, is reported in Table 1. The metal contents loaded on SBA-15 are close to the nominal values, the largest difference being observed for In (4.7%) in the In/Pd/S sample. The results show that coimpregnation method allows to obtain the catalysts with certain metal content.

Table 1
Chemical composition of catalysts.

Sample	Cu	Zn	In	Pd	Fe	K	Si
	(wt.%)						
Cu/Zn/S	18.80	6.09	15.24	5.33			30.59
In/Pd/S							35.03
Fe/K/S					17.36	1.07	36.46

3.2. Structural and Phase Composition Characterization of Catalysts

The ordered mesoporous structure of SBA-15 was observed in all samples by three diffraction reflections on SAXS patterns (Fig. 1. a). A broad reflection between diffraction angles of 15° and 30° on WAXS patterns correspond to amorphous silica of mesoporous SBA-15 (Fig. 1. b). The labels at the positions of the first three reflections of SAXS patterns of ordered mesoporous SBA-15 (Fig. 1. a) show the Miller indices of the corresponding lattice planes [14].

The reflections on the diffraction pattern of Cu/Zn/S were identified belonging to tenorite (CuO, ICDD PDF-2 card number 89-2529). The crystallite size of tenorite, averaged over the two strongest reflections (-111) and (111), was **2.5(5) nm**. The reflections corresponding to ZnO were not observed, most likely due to ZnO being well dispersed into an X-ray amorphous.

Qualitative phase analysis of sample In/Pd/S identified two crystalline phases. The main phase was cubic In_2O_3 (ICDD PDF-2 card number 71-2194), and the second was tetragonal palladinite (PdO, ICDD PDF-2 card number 41-1107). Crystallite size of In_2O_3, averaged over six different crystallographic directions that showed in diffraction pattern the strongest and not overlapping reflections, was **12(2)** nm. A rough estimation of the crystallite size for PdO was possible to give only by comparing the broadening values of reflections from In_2O_3 with a broad (101) reflection from PdO located at diffraction angle 33.8°.

The latter was approximately four times broader, corresponding to the crystallite size approximately **3 nm.**

The only crystalline phase observed in the sample Fe/K/S was hematite (Fe_2O_3, ICDD PDF-2 card number 76-8402). The crystallite size of hematite, averaged over six strongest and not overlapping reflections, was **13(1)** nm.

3.3. Textural characterization

Figure 2. a. exhibits IUPAC type IV isotherms with a H1 hysteresis loop for all three catalysts, corresponding to the mesoporous materials consisting of ordered array of cylindrical pores [15], which indicates that the mesoporous structure of SBA-15 was not damaged after incorporation of the active phases.

Figure 2. b demonstrates that In/Pd/S and Fe/K/S catalysts have a uniform pore size distribution (average diameter 7.8 nm), but the pore size distribution for Cu/Zn/S is uneven. It could be explained by partial pore filling. The surface area of catalysts is similar (see Table 2) – however the Cu/Zn/S has relatively the smallest comparing with others due to the larger metal content loaded, see ICP-AES results, Table 1.

Table 2
Specific surface area, pore diameter, and pore volume of the catalysts.

Sample	BET surface area [m^2/g]	Dpore [nm][a]	Vtotal [cm^3/g][b]
S	554	7.8	0.96
Cu/Zn/S	304	7.9	0.71
In/Pd/S	353	7.8	0.83
Fe/K/S	318	7.9	0.77

a Pore diameters were derived from the desorption branches of the isotherms by using the BJH method

b Total pore volumes were estimated from the absorbed amount at a relative pressure of p/p = 0.99

3.4. Morphology of the Catalysts

Nanoparticles in the size range comparable with SBA-15 pores were visible with STEM for Cu/Zn/S catalyst (see Fig. 3. a). Homogeneous distribution of nanoparticles, seemingly along the pores is apparent and regular dispersion of elements, including loaded metals, was obtained (see STEM-EDX elemental maps in Fig. 3. b-e (oxygen not shown)). STEM confirms partial pore filling for Cu/Zn/S catalyst noticed by N_2 adsorption-desorption isotherms, the images showed that the active phase is distributed on the surface and in the pores.

Particles larger than the size of the pores were obtained with In/Pd/S and Fe/K/S catalysts (see Fig. 4 and Fig. 5). Particle sizes measured with SEM are in line with XRD data, which also showed that crystallite size of In_2O_3 and hematite was similar. We can conclude that these two samples have similar particle size, whereas smaller nanoparticles can be obtained with Cu/Zn/S catalyst.

3.5. Reducibility of catalysts

TPR profile of the Cu/Zn/S catalyst shows a well-defined peak with a maximum corresponding to 320°C (Fig. 6. a), which is ascribable to the reduction of CuO to metallic copper. Upon closer inspection, a tailing of the peak towards low temperatures is observed, suggesting the overlapping of different contributions. For a CuO/ZnO catalyst, Shozi and co-authors [16] reported a TPR profile showing two peaks at 292 and 340°C, which were ascribed to the reduction of CuO through the following steps: $CuO \rightarrow Cu_2O \rightarrow Cu^0$. Accordingly, a two-steps reduction of copper oxide may also occur in the present case.

The reduction profile of the In/Pd/S sample (Fig. 6. b) shows a negative peak at about 90°C followed by two intense partially overlapping peaks at ca. 440 and 650°C, which are made up of different contributions, as suggested by their asymmetrical and enlarged shape. A less intense feature is also observable at ca. 880°C. According to the literature [17,18,19,20] the negative peak at low temperature can be ascribed to the decomposition of Pd β-hydrides formed on Pd^0 deriving from the reduction of PdO_x clusters, which are reduced at low temperatures [19,20], lower than the starting temperature adopted for these TPR analyses. The shoulder appearing in the temperature range 200−300°C can be attributed to the reduction of surface In_2O_3 and the formation of oxygen vacancies [6,22], whereas peaks at higher temperatures can be ascribed to the reduction of bulk In_2O_3 [8].

The Fe/K/S sample (Fig. 6. c) shows a very complex TPR profile consisting of several unresolved peaks in the temperature range 400−950°C. Similar reduction features were observed for SBA-15-suppored Fe-based catalysts by Cano and co-workers [21], who ascribed such a complex profile to the reduction of Fe^{3+} and Fe^{2+} species in oxides particles of different sizes and with different interactions with the silica support. Moreover, in the case of a K-promoted sample, they also observed a contribution at very high temperatures (>720°C), which was ascribed to the formation of K^+ ionic species on the SBA-15 surface. The appearance of the numerous reduction peaks in the TPR profile of the present Fe/K/S sample can be explained accordingly.

For the Cu/Zn/S, In/Pd/S, and Fe/K/S catalysts, the extent of reduction (%) was calculated from the amount of hydrogen consumed during TPR analyses by considering stoichiometric $Me^{n+}:H_2$ ratios equal to 1:1 ($Me = Cu^{2+}$) or 2:3 ($Me = In^{3+}, Fe^{3+}$). The obtained values were 100, 79, and 65%, indicating that the reducibility of the Me^{n+} species decreases in the order $Cu^{2+} > In^{3+} > Fe^{3+}$.

3.6. Basicity of catalysts

The surface basic properties of the prepared samples were investigated by CO_2-TPD, and the results are shown in Fig. 7. According to the literature [22], desorption peaks at lower temperatures (50−300°C) are

ascribable to CO_2 interacting with weak (α-type) and medium strength (β-type) basic sites, related to OH⁻ groups and to metal–oxygen pairs, respectively [23]; strong basic sites (γtype), responsible for desorption peaks at higher temperatures, are instead associated with low-coordination oxygen atoms [23]. The TPD profile of Cu/Zn/S presents only one peak with a maximum corresponding to 480°C (Fig. 7.), which is indicative of the presence of strong basic sites. On the contrary the other two samples show contributions in a wider interval of temperatures (80–500°C), which point out the presence of sites in the whole range of basic strength. The amount of adsorbed CO_2, estimated from the peak area after calibration of the TCD response, was 20, 109, and 55 mmol/g for Cu/Zn/S, In/Pd/S, and Fe/K/S, respectively.

3.7. Catalytic Activity

The catalysts were tested in the CO_2 hydrogenation reaction under the same reaction conditions, 250°C, 20 bar, H_2 to CO_2 molar ratio 4 to 1. The results are reported in Fig. 8 and Fig. 9. The highest catalytic activity was shown by the Cu/Zn/S catalyst, for which CO_2 conversion reached 21.3% and STY was 288 mg_{CH3OH} h^{-1} g_{cat}^{-1}. For this type of catalyst it is high value, Mureddu et al. obtained 158 mg_{CH3OH} h^{-1} g_{cat}^{-1} using harsher reaction conditions (30 bar)[4]. Cu/Zn/S catalyst showed high activity during the whole reaction time (50 hours) (see Fig. 8). The obtained results could be explained by the presence of strong basic sites in Cu/Zn/S. It is known that surface basicity enhances CO_2 adsorption and promotes CO_2 conversion, as well as it can increase methanol selectivity [24]. This high activity can also be attributed to the good dispersion of the tenorite and zinc oxide phases and the small size of the nanoparticles.

In/Pd/S showed lower activity for methanol production than Cu/Zn/S – the CO_2 conversion was 3.1%, and the methanol yield (3 mg_{CH3OH} h^{-1} g_{cat}^{-1}) obtained was extremely lower than that of Cu/Zn/S catalyst. In addition, the In/Pd/S catalyst showed lower methanol selectivity as it produced also 9% methane (see product distribution in gaseous phase, Fig. 9). This can be attributed to the lower reducibility of In^{3+} than Cu^{2+} and the metal-support interaction – for In/Pd/S catalyst the particles are larger and distributed mainly on the surface of the SBA-15.

Fe/K/S catalyst showed the lowest activity (CO_2 conversion 0.8%) in CO_2 hydrogenation reaction, the main product obtained was methane (see Fig. 9). The CO_2 hydrogenation reaction results of Fe/K supported on SBA-15 showed that the metal-support interaction affected the properties of this catalyst, resulting in methane as the main reaction product, similarly to FischerTropsch synthesis at temperatures below 250°C [25].

4. Conclusions

Three different catalytic systems were synthesized using mesoporous silica SBA-15 as a support material by co-impregnation method: copper-based catalyst with zinc, indium-based catalyst with palladium and iron-based catalyst with potassium. The characterization showed that main phases obtained were tenorite, palladinite, indium oxide and hematite, respectively. ICP-AES results showed that Cu/Zn catalytic system is the most appropriate for loading on SBA-15 support, as practically all metal amount calculated

was loaded. Catalyst characterization showed that the smallest nanoparticles, the good dispersion of metal oxide phases and the highest reducibility can be obtained with Cu/Zn/S catalyst. CO_2-TPD data showed presence of strong basic sites for Cu/Zn/S. It resulted with the highest methanol yield in CO_2 hydrogenation reaction, 0.035 g/h at 250°C, 20 bar, H_2 to CO_2 molar ratio 4 to 1 using fixed-bed tubular micro-activity reactor.

Declarations

Declaration of interests

The authors declare that they have no known competing financial interests or personal relationships that could have appeared to influence the work reported in this paper.

References

1. T. A. Atsbha, T. Yoon, P. Seongho, C. J. Lee, J. CO2 Util. 44 (2021), 101413, doi: 10.1016/j.jcou.2020.101413.
2. K. Stangeland, H. Li, Z. Yu, Energy, Ecol. Environ. 5(4) (2020) 272–285, doi: 10.1007/s40974-020-00156-4.
3. X. Xi *et al.*, ACS Sustain. Chem. Eng. 9(18) (2021) 6235–6249, doi: 10.1021/acssuschemeng.0c08760.
4. M. Mureddu, F. Ferrara, A. Pettinau, Appl. Catal. B Environ. 258 (2019) 117941, doi: 10.1016/j.apcatb.2019.117941.
5. H. Chen *et al.*, Fuel 314 (2022) 123035, doi: 10.1016/j.fuel.2021.123035.
6. H. Jiang, J. Lin, X. Wu, W. Wang, Y. Chen, M. Zhang, J. CO2 Util. 36 (2020) 33–39, doi: 10.1016/j.jcou.2019.10.013.
7. Z. Li *et al.*, Appl. Surf. Sci. 603 (2022) 154420, doi: 10.1016/j.apsusc.2022.154420.
8. N. Rui, Z. Wang, K. Sun, J. Ye, Q. Ge, C. jun Liu, Appl. Catal. B Environ. 218 (2017) 488–497, doi: 10.1016/j.apcatb.2017.06.069.

9. J. Ye, C. Liu, D. Mei, Q. Ge, ACS Catalysis 3 (6) (2013) 1296–1306, doi: 10.1021/cs400132a.

10. R. Yao *et al.*, *A*ppl. Catal. B Environ. 298 (2021) 120556, doi: 10.1016/j.apcatb.2021.120556.

11. D. Xu, M. Ding, X. Hong, G. Liu, ACS Catal. 10 (24) (2020) 14516–14526, doi: 10.1021/acscatal.0c03575.

12. D. Mao, J. Zhang, H. Zhang, D. Wu, Catal. Today 402 (2022) 60–66, doi: 10.1016/j.cattod.2022.03.002.

13. Z. Abelniece, V. Kampars, H. M. Piirsoo, H. Mändar, A. Tamm, Environ. Prog. Sustain. Energy, 41 (5) (2022) 1–9, doi: 10.1002/ep.13905.

14. D. Zhao *et al.*, Science (80-.). 279(5350) (1998) 548–552, doi: 10.1126/science.279.5350.548.

15. Z. A. Alothman, Materials (Basel). 5 (12) (2012) 2874–2902, doi: 10.3390/ma5122874.

16. M. L. Shozi *et al.*, Sustain. Energy Fuels 1 (6) (2017) 1437–1445, doi: 10.1039/C7SE00199A.

17. C. M. Mendez, H. Olivero, D. E. Damiani, M. A. Volpe, Appl. Catal. B Environ. 84 (1–2) (2008) 156–161, doi: 10.1016/j.apcatb.2008.03.019.

18. J. Batista, A. Pintar, D. Mandrino, M. Jenko, V. Martin, Appl. Catal. A Gen. 206 (1) (2001) 113–124, doi: 10.1016/S0926-860X(00)00589-5.

19. J. Zheng, M. Guo, C. Song, Fuel Process. Technol. 89(4) (2008) 467–474, doi: 10.1016/j.fuproc.2007.11.025.

20. S. Echeandia *et al.*, Fuel, 117 (2014) 1061–1073, doi: 10.1016/j.fuel.2013.10.011.

21. L. A. Cano, A. A. Garcia Blanco, G. Lener, S. G. Marchetti, K. Sapag, Catal. Today 282 (2017) 204–213, doi: 10.1016/j.cattod.2016.06.054.

22. W. Wang, Z. Qu, L. Song, Q. Fu, "CO2 hydrogenation to methanol over Cu/CeO2 and Cu/ZrO2 catalysts: Tuning methanol selectivity via metal-support interaction," *J. Energy Chem.*, vol. 40, pp. 22–30, 2020, doi: 10.1016/j.jechem.2019.03.001.

23. P. Gao *et al.*, J. Catal. 298 (2013) 51–60, doi: 10.1016/j.jcat.2012.10.030.

24. S. Li, Y. Wang, B. Yang, L. Guo, Appl. Catal. A Gen. 571 (2019) 51–60, doi: 10.1016/j.apcata.2018.12.008.

25. C. F. Toncón-Leal, J. F. Múnera, J. J. Arroyo-Gómez, K. Sapag, Catal. Today 394–396 (2022) 150–160, doi: 10.1016/j.cattod.2021.07.023.
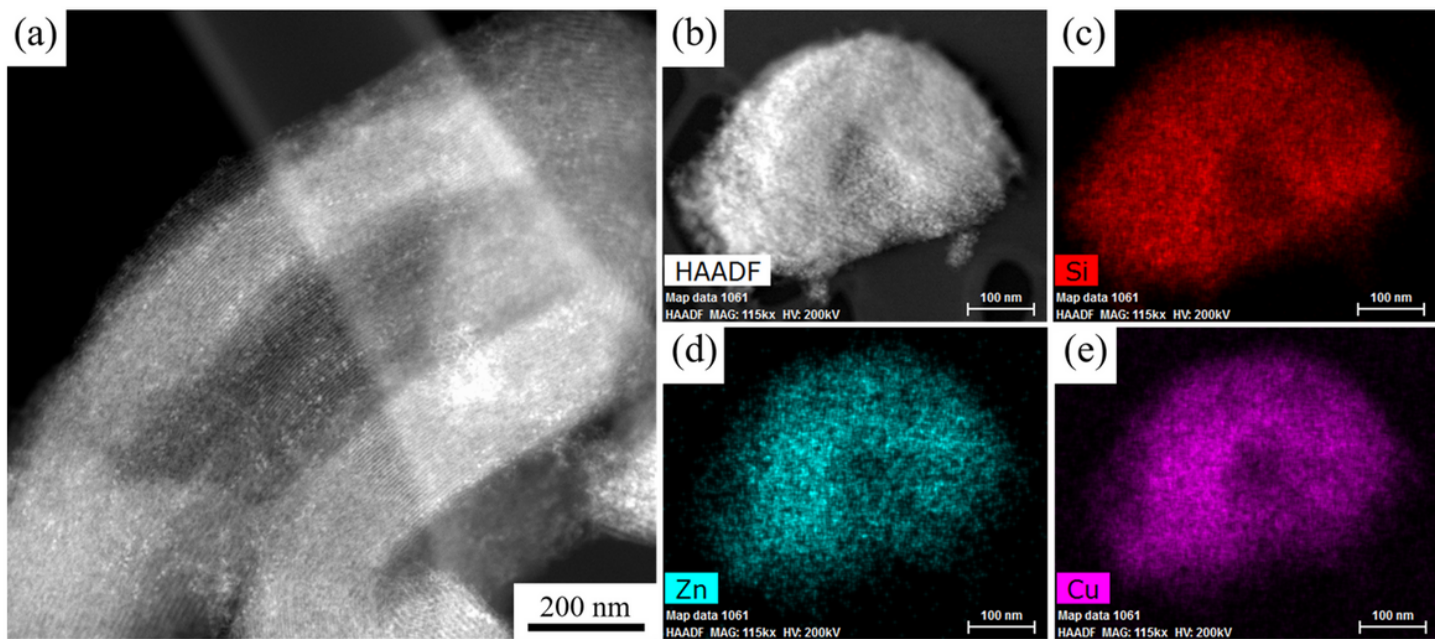
Figures
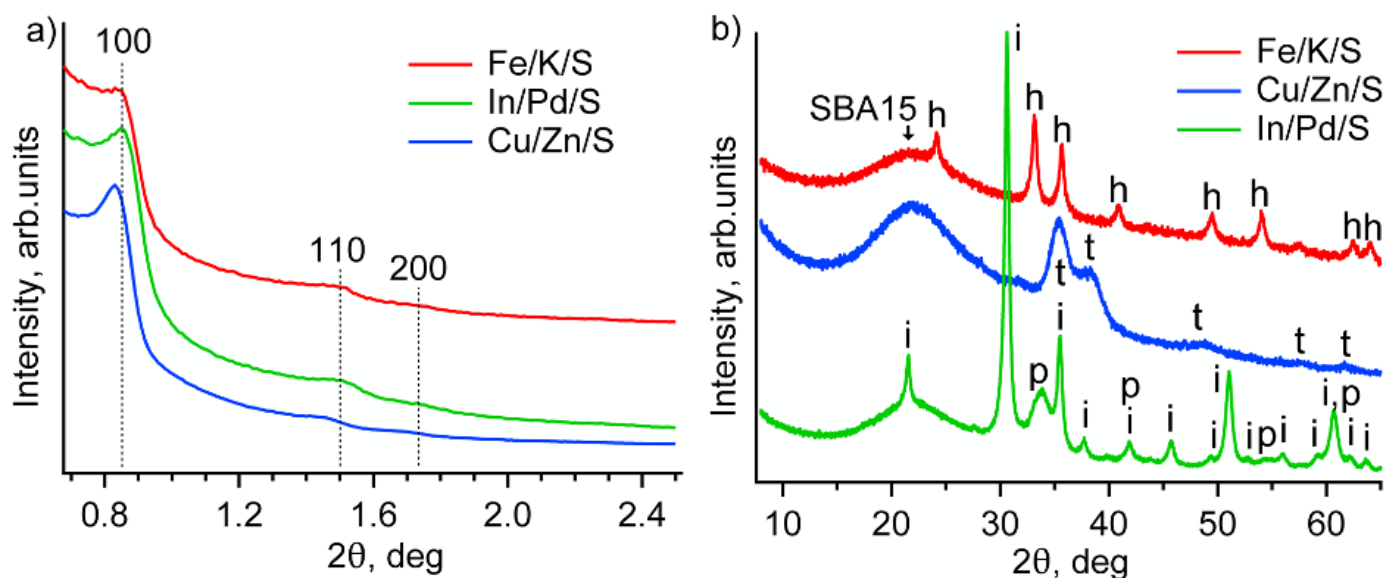
Figure 1

a. Transmission SAXS patterns of samples. b. WAXS patterns of samples. The reflections of SBA-15, tenorite, palladinite, hematite and In_2O_3 are marked with SBA-15, t, p, h and i, correspondingly. A vertical offset of patterns was applied to avoid overlapping.
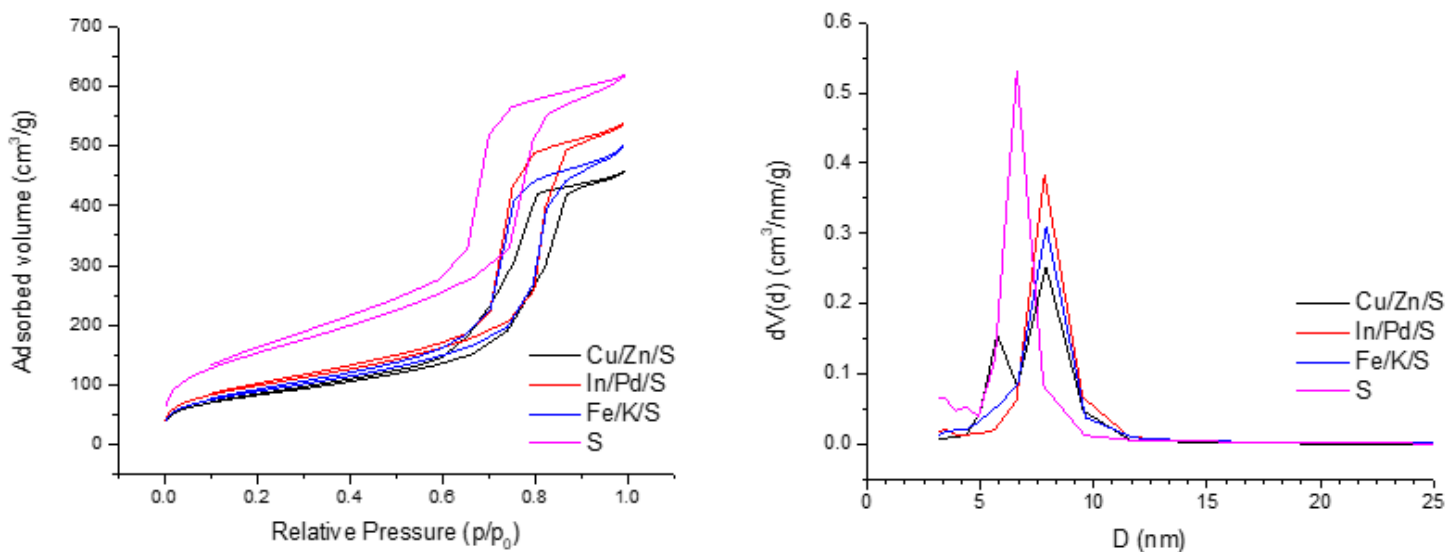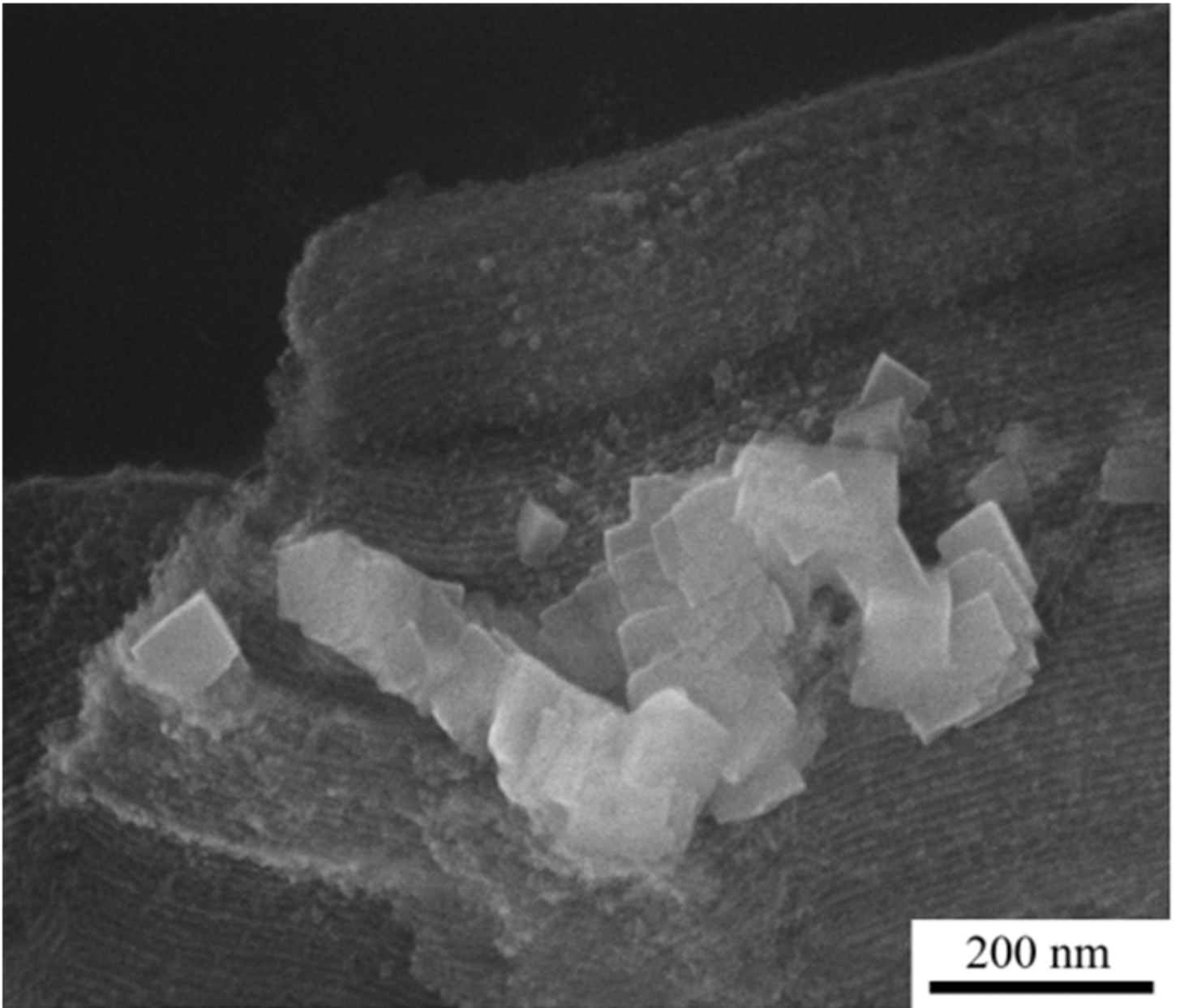

Figure 2

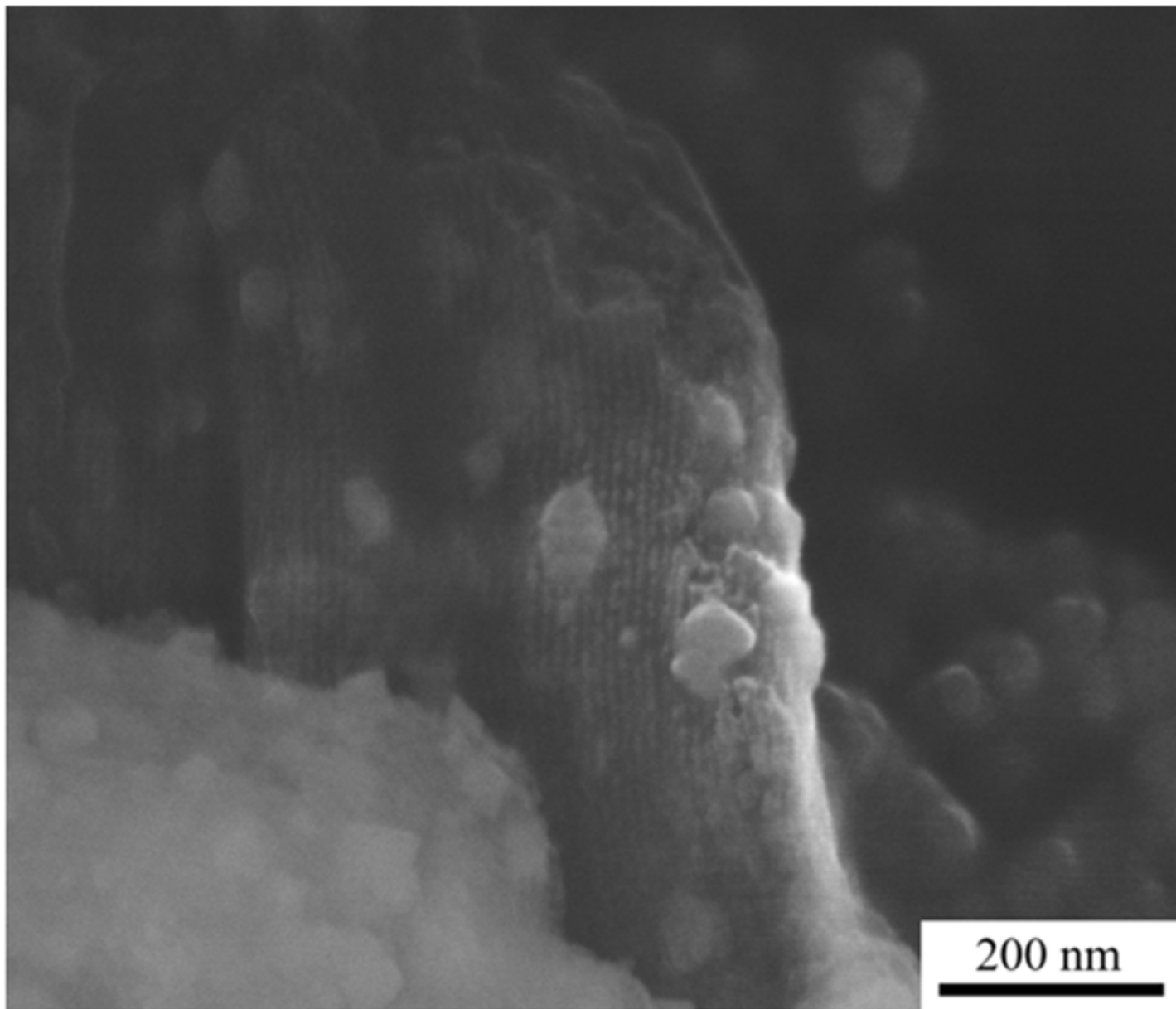a. N_2 adsorption-desorption isotherms. b. Pore size distribution of catalysts.

Figure 3

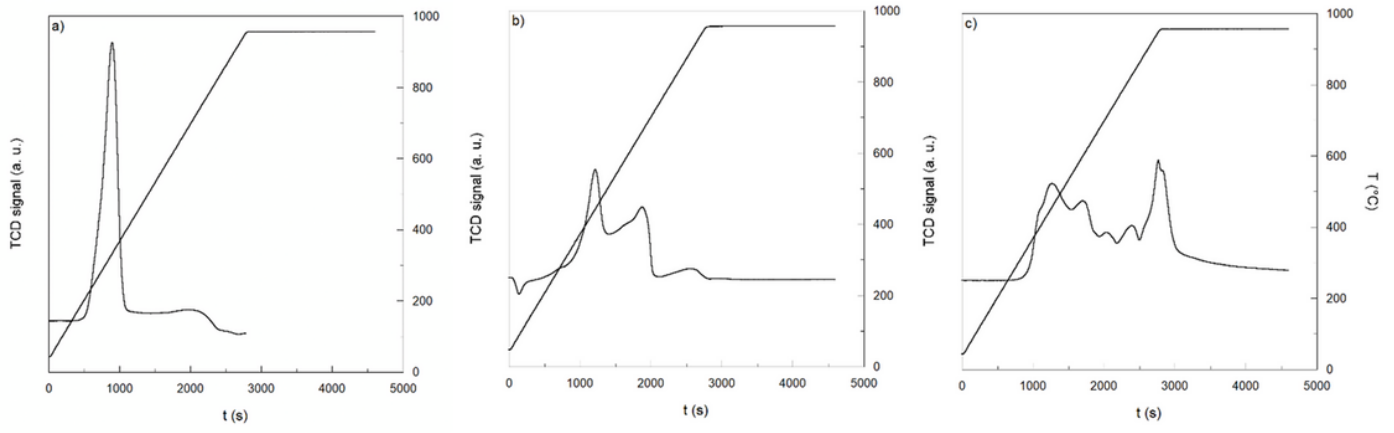a. STEM image of **Cu/Zn**/S catalyst; Fig.3. b-e. STEM-EDX elemental mapping of **Cu/Zn**/S catalyst.

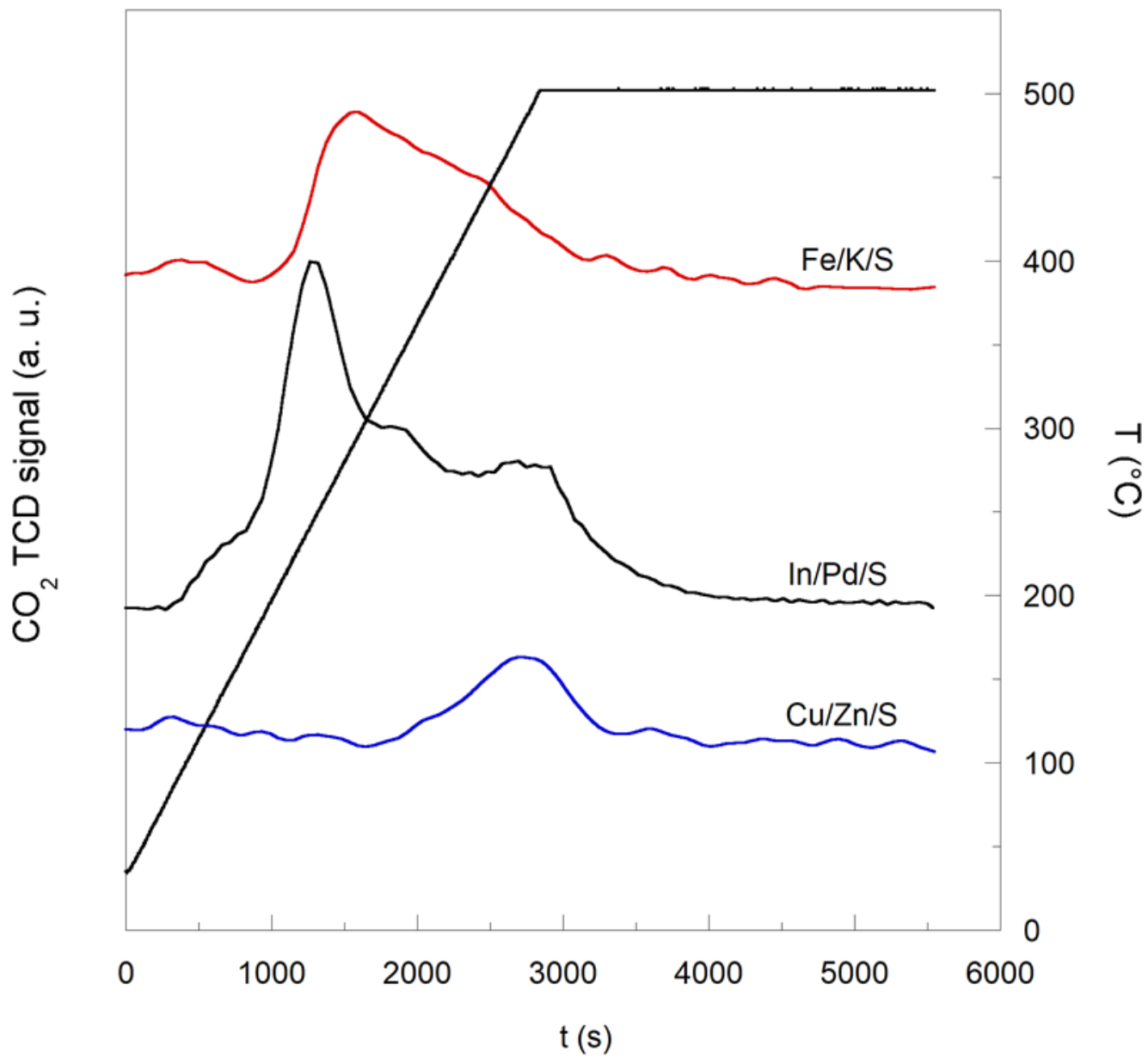**Figure 4**

SEM image of In/Pd/S catalyst.

Figure 5

SEM image of Fe/K/S catalyst.

Figure 6

TPR profiles of the as-prepared catalysts: a. Cu/Zn/S; b. In/Pd/S; c. Fe/K/S.

Figure 7

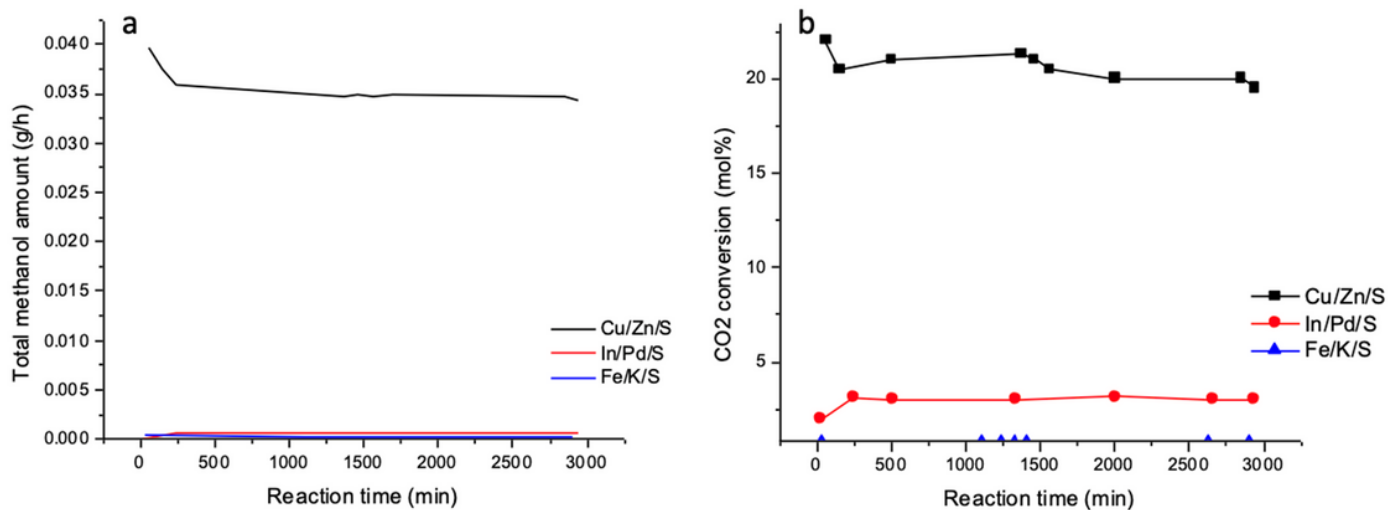CO_2-TPD profiles of the as prepared catalysts.

Figure 8

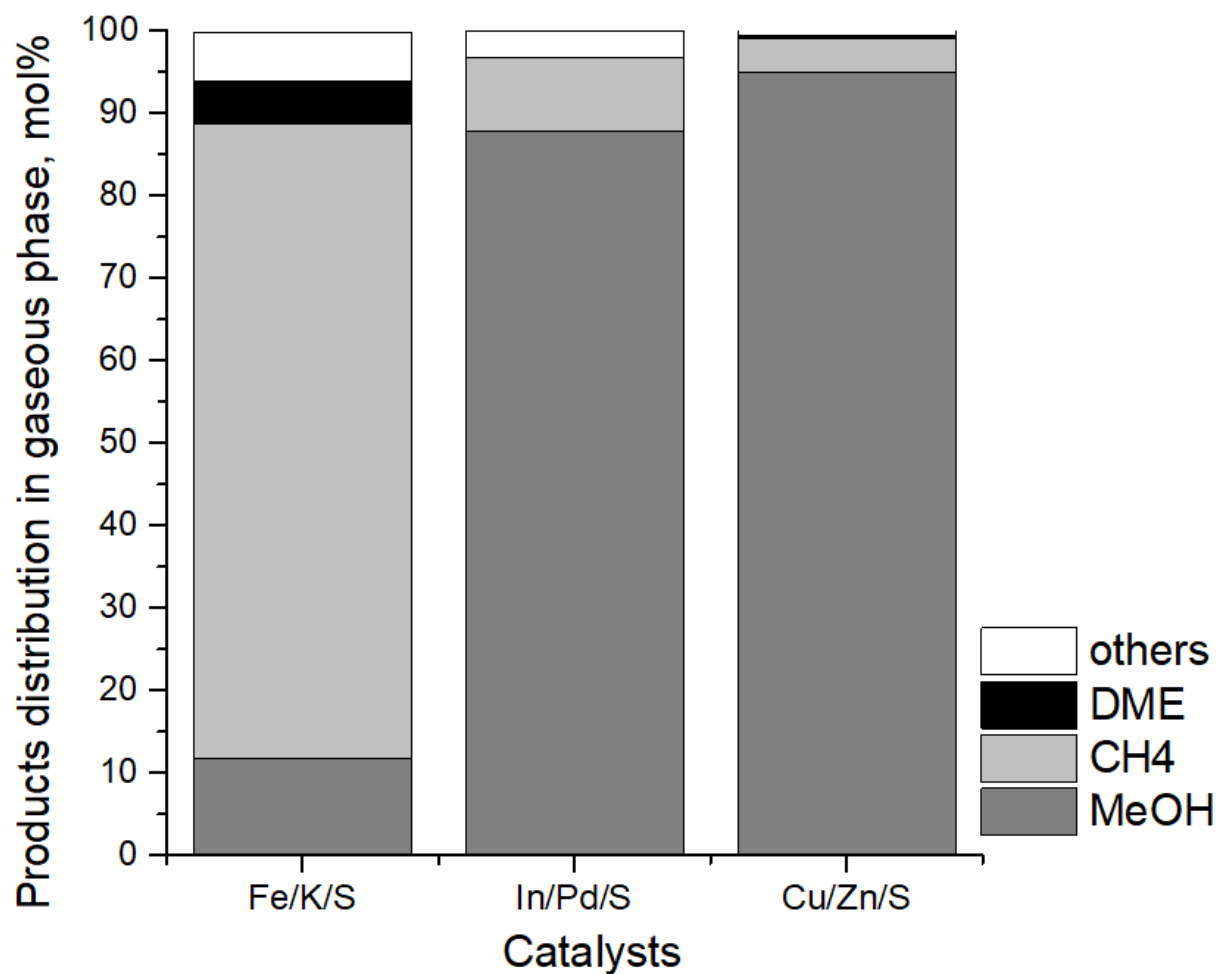Catalytic activity: a. total methanol amount obtained, b. CO_2 conversion efficiency against reaction time.

Figure 9

Product distribution in gaseous phase.